



Prediction of Dry-Wet-Dry Transition in Polymer Electrolyte Fuel Cells

Gang Luo, Hyunchul Ju, and Chao-Yang Wang^{*,z}

Electrochemical Engine Center and Department of Mechanical and Nuclear Engineering,
The Pennsylvania State University, University Park, Pennsylvania 16802 USA

Condensation and evaporation fronts co-exist in present-day automotive polymer electrolyte fuel cells (PEFCs) where low-humidity reactant gases are fed in counterflow. Capturing of such a transition between a single- and a two-phase regime is not only of technological significance, but also represents a great numerical challenge in PEFC modeling. In this work we demonstrate a computational capability to predict the dry-wet-dry transition in a PEFC based on the multiphase mixture (M^2) framework. The M^2 model is a three-dimensional, two-phase, and multicomponent full-cell model featuring a detailed membrane-electrode assembly (MEA) sub-model. Three-dimensional results on the dry-wet-dry transition under low-humidity operation and in counterflow are presented. The dry-to-wet transition described in this work provides a benchmark problem to develop and test future generation PEFC models.

© 2007 The Electrochemical Society. [DOI: 10.1149/1.2429036] All rights reserved.

Manuscript submitted September 6, 2006; revised manuscript received October 31, 2006.
Available electronically January 17, 2007.

Low-humidity operation is ubiquitous in automotive polymer electrolyte fuel cells (PEFCs). Under low-humidity inlet conditions, reactant gases undergo a transition from the single-phase to two-phase flow inside the fuel cell when either anode or cathode gas becomes saturated with water vapor due to water production from oxygen reduction reaction. This transition, also called the condensation front, is schematically sketched in Fig. 1. In the counterflow of hydrogen and air gas streams at low humidity, the most common configuration of automotive PEFCs, there may occur a second transition from the two-phase zone back to the single-phase gas flow, or the evaporation front, also depicted in Fig. 1. The evaporation front results from the wet cathode outlet facing the dry anode inlet such that not only is product water from oxygen reduction reaction (ORR) transported through the membrane to the dry anode gas, but liquid water accumulated in the cathode GDL also vanishes due to strong water diffusion through the membrane to the dry anode. Commonly, both fronts (i.e., the dry-wet-dry transition) can exist simultaneously in the PEFC cathode and anode.

Predicting the dry-wet-dry transition (DWT) is of great importance to PEFC performance and durability as the ultimate goal of water management is precisely met in the vicinity of a DWT. Here, the membrane is sufficiently hydrated to exhibit excellent proton conductivity, and yet the electrodes have not been flooded. However, despite its technological importance and existence in virtually all automotive PEFC engines, the DWT has been scarcely studied due to the tremendous numerical difficulty in capturing it. Falling into the general category of moving boundary problems,¹ the location of DWT is unknown a priori and must be found as part of the solution. Most papers²⁻⁴ on two-phase modeling of PEFCs avoided this problem by focusing on cases with fully humidified reactant streams at the inlet, where DWT is absent. Berning and Djilali used a two-fluid model, while Mazumder and Cole as well as Meng and Wang applied the multiphase mixture (M^2) model originally developed by Wang and Cheng⁵ for general porous media and later applied to PEFCs by Wang et al.⁶ The only works in the literature that have examined DWT to a limited extent are due to Wang et al.⁶ and Pasaogullari and Wang,⁷ both of which were based on the M^2 model and explored DWT in the two-dimensional domain only. In addition, the evaporation front has never been predicted in the literature.

While the two-fluid model and M^2 model are mathematically equivalent, the M^2 model eliminates the need to track the interface between single- and two-phase regions, and thus is theoretically suitable for the numerical capturing of DWT using fixed grids without resorting to complex front tracking algorithms. The objective of

this work is to fully demonstrate this salient feature of the M^2 model in capturing DWT in three-dimensional, full-cell simulations under various inlet RH conditions. We shall show that the prediction of DWT is readily available in routine simulations for PEFC design.

Numerical Model

The two-phase PEFC model used in this work is based on the M^2 model originally of Wang and Cheng⁵ and later extended to the fuel cell application by Wang et al.⁶

Model assumptions.— Utilizing the M^2 formulation for two-phase transport, the present two-phase PEFC model invokes the following assumptions: (i) ideal gas mixtures, (ii) laminar flow due to small flow velocities, (iii) isotropic and homogeneous porous media, characterized by an effective porosity and a permeability, and (iv) two-phase mist flow (i.e., homogeneous flow) in gas channels assuming that there exist only tiny water droplets that travel at the same velocity as the gas.

Conservation equations.— The energy equation is ignored in the present work for clarity of presentation. Nonisothermal, two-phase modeling has been described elsewhere.⁸ With the above assumptions, the governing equations of mass, momentum, species, proton and electron transport in the M^2 model can be stated as

$$\nabla \cdot (\rho \vec{u}) = S_m \quad [1]$$

$$\frac{1}{\varepsilon^2} \nabla \cdot (\rho \vec{u} \vec{u}) = -\nabla p + \nabla \cdot \tau - \frac{\mu}{K} \vec{u} \quad [2]$$

$$\nabla \cdot (\gamma_i \rho m_i \vec{u}) = \nabla \cdot [\rho^g D_i^{g,eff} \nabla (m_i^g)] + \nabla \cdot [(m_i^g - m_i^l)^2] + S_i \quad [3]$$

$$\nabla \cdot (\kappa^{eff} \nabla \phi_e) + j = 0 \quad [4]$$

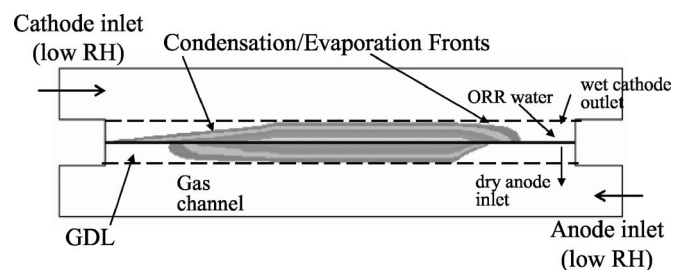


Figure 1. Schematic of dry-wet-dry transition in a PEFC with the gray region denoting the two-phase zone with liquid water.

* Electrochemical Society Active Member.

^z E-mail: cwx31@psu.edu

$$\nabla \cdot (\sigma^{eff} \nabla \phi_s) - j = 0 \quad [5]$$

Derivation details of the above equations can be found in Wang,⁹ Wang and Wang,¹⁰ Pasaogullari and Wang,⁷ Meng and Wang,⁴ and thus are not repeated here. Note, however, that in porous layers, instead of solving the full Navier-Stokes equation with a source term in our previous work, we choose to solve the following Darcy's law in the present work

$$\rho \vec{u} = - \frac{K}{\nu} \nabla p \quad [6]$$

Also, the species equation is written in terms of mass fraction in this work instead of molar concentration as in our previous work. As a result, we do not solve for the molar concentration in the membrane but for the water content, λ , from the following water conservation equation

$$\nabla \cdot \left(\frac{\rho^{mem}}{EW} D_w^{mem} \nabla \lambda \right) M_w - \nabla \cdot \left(n_d \frac{I}{F} \right) M_w + \nabla \cdot \left(\frac{K^{mem}}{\nu^l} \nabla P^l \right) = 0 \quad [7]$$

where K^{mem} is the hydraulic permeability of the membrane. In numerical simulations, we have assumed a linear profile in liquid pressure across the membrane and hence the gradient ∇P^l in Eq. 7 can be estimated from values at the interfaces of the membrane with the anode and cathode catalyst layers.

Two-phase parameters.— Liquid saturation is a key factor in a two-phase flow model. Here we can calculate the liquid saturation from the mixture mass fraction of water

$$s = \frac{\rho m_w - C_{sat} M_w}{\rho^l - C_{sat} M_w} \quad [8]$$

Other two-phase mixture relations are listed below.⁵ Two-phase mixture density and velocity

$$\rho = \rho^l \cdot s + \rho^g \cdot (1 - s) \quad [9]$$

$$\rho \vec{u} = \rho^l \vec{u}^l + \rho^g \vec{u}^g \quad [10]$$

The relative permeability of liquid and gas phase

$$k_r^l = s^4, \quad k_r^g = (1 - s)^4 \quad [11]$$

Two phase mixture kinematic viscosity

$$\nu = \left(\frac{k_r^l}{\nu^l} + \frac{k_r^g}{\nu^g} \right)^{-1} \quad [12]$$

The mobility of liquid and gas phase

$$\lambda^l = \frac{k_r^l}{\nu^l}, \quad \lambda^g = 1 - \lambda^l \quad [13]$$

The diffusive mass flux of liquid phase, \vec{j}^l

$$\vec{j}^l = \rho^l \vec{u}^l - \lambda^l \rho \vec{u} = \frac{K}{\nu} \lambda^l \lambda^g \nabla P_c \quad [14]$$

The capillary pressure, P_c can be further expressed as⁵

$$P_c = P^g - P^l = \sigma \cos \theta \left(\frac{\varepsilon}{K} \right)^{1/2} J(s) \quad [15]$$

where $J(s)$ is the Leverett function, which can be expressed for both hydrophobic and hydrophilic porous layers as⁵

$$J(s) = \begin{cases} 1.417(1-s) - 2.120(1-s)^2 + 1.263(1-s)^3 & \text{if } \theta_c < 90^\circ \\ 1.417s - 2.120s^2 + 1.263s^3 & \text{if } \theta_c > 90^\circ \end{cases} \quad [16]$$

Individual phase velocities can be calculated according to the following relations after a solution is obtained

$$\rho^l \vec{u}^l = \vec{j}^l + \lambda^l \rho \vec{u} \quad \text{and} \quad \rho^g \vec{u}^g = - \vec{j}^l + \lambda^g \rho \vec{u} \quad [17]$$

Source terms and physicochemical relations.— In the water and oxygen species equations, the source terms resulting from electrochemical kinetics in the catalyst layer can be expressed as follows

$$S_i = M_i \left[- \frac{s_i j}{nF} - \nabla \cdot \left(\frac{n_d}{F} I \right) \right] \quad [18]$$

In the above equation, the electro-osmotic drag term is only relevant to the water equation and appears inside the membrane and catalyst layers.

The nonzero mass source/sink in the continuity equation, S_m , arises from the summation of all species equations

$$S_m = \sum_i S_i + M_w \nabla \cdot \left(D_w^{mem} \frac{\rho^{mem}}{EW} \nabla \lambda \right) \quad [19]$$

A detailed description of this mass source/sink can be found in Wang and Wang¹⁰ and Wang.⁹ The source term S_m and varying gas density with compositions represent two critical couplings between the flow field and species distribution with electrochemical reaction.

The transfer current densities are represented by kinetic expressions as follows

$$\text{Anode CL} \quad j = (1 - s)^{n_c} a_{0,a}^{ref} \left(\frac{C_{H_2}}{C_{H_2,ref}} \right)^{1/2} \left(\frac{\alpha_a + \alpha_c}{R_u T} F \eta \right) \quad [20]$$

$$\text{Cathode CL} \quad j = - (1 - s)^{n_c} a_{0,c}^{ref} \left(\frac{C_{O_2}}{C_{O_2,ref}} \right)^{3/4} \exp \left(- \frac{\alpha_c}{R_u T} F \eta \right) \quad [21]$$

where $(1 - s)^{n_c}$ is to approximate the effect of decreasing the electrochemically active catalyst sites due to the presence of liquid water in the catalyst layers.

The surface overpotentials are defined as

$$\text{Anode CL} \quad \eta = \phi_s - \phi_e$$

$$\text{Cathode CL} \quad \eta = \phi_s - \phi_e - U_o$$

where the thermodynamic equilibrium potential is given by¹¹

$$U_o = 1.23 - 0.9 \times 10^{-3} \cdot (T - 298.15) \quad [22]$$

The transport properties of electrolytes are correlated with the water content of the membrane, λ , which in turn is a function of water activity, a , as follows¹²

$$a = \frac{C_w^g R_u T}{P_{sat}} \quad [23]$$

$$\lambda = \begin{cases} 0.043 + 17.81a - 39.85a^2 + 36.0a^3 & \text{for } 0 < a \leq 1 \\ 14 + 8s & \text{for } 0 < s < 1 \text{ in equilibrium with two-phase} \end{cases} \quad [24]$$

The electro-osmotic drag coefficient, n_d , water diffusion coefficient in the membrane, D_w^{mem} , and proton conductivity in the membrane, κ , are given by Springer et al.¹²

$$n_d = \frac{2.5\lambda}{22} \quad [25]$$

$$D_w^{mem} = \begin{cases} 2.692661843 \cdot 10^{-10} & \lambda \leq 2 \\ [0.87(3 - \lambda) + 2.95(\lambda - 2)] \cdot 10^{-10} \cdot e^{2416[(1/303)-(1/T)]} & 2 < \lambda \leq 3 \\ [2.95(4 - \lambda) + 1.642454(\lambda - 3)] \cdot 10^{-10} \cdot e^{2416[(1/303)-(1/T)]} & 3 < \lambda \leq 4 \\ (2.563 - 0.33\lambda + 0.0264\lambda^2 - 0.000671\lambda^3) \cdot 10^{-10} \cdot e^{2416[(1/303)-(1/T)]} & 4 < \lambda \leq 14 \end{cases} \quad [26]$$

$$\kappa = (0.5139\lambda - 0.326)\exp\left[1268\left(\frac{1}{303} - \frac{1}{T}\right)\right] \quad [27]$$

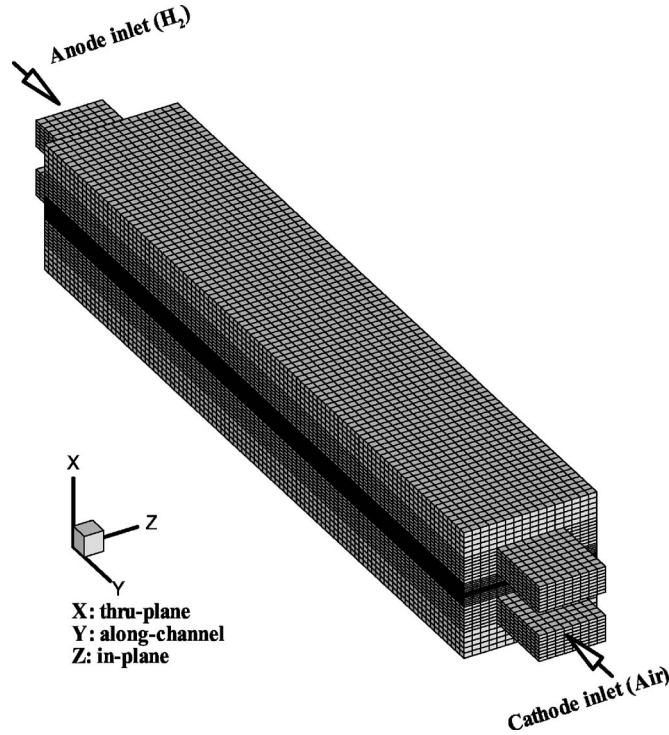


Figure 2. Cell geometry and computational mesh.

The present two-phase PEFC model described above is implemented into a commercial flow solver, STAR-CD,¹³ and has full multidimensional capability. Conventional fixed rectangular Cartesian mesh is employed. A typical simulation with both condensation and evaporation fronts involved in the problem domain requires 1500 to 2000 iterations to meet the convergence criteria of less than 1% global mass imbalance, and takes 10 h CPU time on a single PC (2.8 GHz) for the single-channel 3D geometry shown in the next section with 111,360 cells ($68 \times 100 \times 16$). This computational performance remains virtually the same as that without DWT involved in computations.

Results and Discussion

A single straight-channel PEFC is considered as shown in Fig. 2. Because the 3D two-phase model employed in this work is a comprehensive one, the modeling domain consists of all components of a complete cell, including bipolar plates, gas channels, gas diffusion layers (GDLs), and catalyst layers on both anode and cathode sides, as well as the membrane. The geometries of various components and other relevant physicochemical and transport parameters are listed in Table I and II, respectively. A constant average current density of 1.5 A/cm^2 is applied as a boundary condition following the work of Meng and Wang,¹⁴ and a stoichiometric flow ratio of 2 is used at both anode and cathode inlets. This means that the reactant flow rates are equivalent to 3 A/cm^2 . The cell operates at 80°C and 1.5 atm. Unless noted otherwise, 50% anode and 50% cathode inlet

Table I. Geometrical and operating parameters.

Description	Value
Cell length	70.0 mm
Gas channel depth	0.5 mm
Gas channel width	1.0 mm
Land width	1.0 mm
Anode/cathode DM thickness	0.210 mm
Anode/cathode catalyst layers thickness	0.010 mm
Membrane thickness	0.018 mm
Porosity of anode/cathode DM, ε_{DM}	0.6
Porosity of anode/cathode catalyst layers, ε_{CL}	0.6
Volume fraction of ionomer in anode/cathode catalyst layers, ε_e	0.18
Hydraulic permeability of anode/cathode DM, K_{DM}	$3.0 \times 10^{-12} \text{ m}^2$
Hydraulic permeability of membrane, K_{mem}	$5.0 \times 10^{-20} \text{ m}^2$
Contact resistance between catalyst layer and DM, R_{CDM}	$1.0 \times 10^{-6} \Omega \cdot \text{m}^2$
Anode/cathode inlet pressure, P_{in}	1.5 atm
Cell temperature, T_{cell}	80°C
Anode/cathode stoichiometry, ξ_a/ξ_c	2/2

relative humidity are chosen for the base case. All the plots are drawn not to scale for better view in Fig. 3 through 8.

Figures 3a and b show the gas velocity vectors in the anode and cathode GDL under the center of the gas channels in the through-plane direction. Figure 3c shows the water content distribution in the membrane under the center of the gas channels in the through-plane direction. The interface between single- and two-phase regions is represented by a thick solid iso-line of $s = 1\%$. There is no two-phase region under the anode gas channel. In region A, where the cathode side of the membrane is drier than the anode side, forward diffusion of water aids in electro-osmotic drag (EOD), resulting in the net water flux from the anode to cathode. Thus, the gas velocity points from the anode to cathode. In regions B and C, where the anode side of the membrane is drier than the cathode, back diffusion opposes the EOD flux. It is seen that the gas velocity in the anode GDL points toward the cathode in Region B, thus implying a net water flux toward the cathode as dominated by EOD flux. With water being continuously produced from ORR and transported through the membrane from the anode, more liquid water appears as region B transitions to region C. In region C, the gas velocity in the anode GDL reverses its direction and begins to point toward the anode gas channel, signifying the dominance of water back diffusion. The net water flux becomes toward the anode. As the back diffusion through the membrane strengthens along the cathode flow direction in region C due to drier anode gas near the inlet, ORR-produced water is no longer sufficient to sustain the membrane water flux drawn to the anode, and liquid water in the cathode GDL begins to disappear. Consequently, the wet cathode GDL is transitioned back to the single-phase towards the cathode outlet, creating the second DWT. Note that both gases, entering the cell dry, are internally humidified. This is a distinct advantage of the counterflow configuration.

Table II. Physicochemical parameters.

Description	Value
Exchange current density \times ratio of reaction surface to catalyst layer volume in anode side, $a_{0,a}^{ref}$	$1.0 \times 10^9 \text{ A/m}^3$
Exchange current density \times ratio of reaction surface to catalyst layer volume in cathode side, $a_{0,c}^{ref}$	$2.0 \times 10^4 \text{ A/m}^3$
Activation energy for oxygen reduction reaction in cathode side, E_a	73269 J/mol
Reference hydrogen molar concentration, $c_{H_2,ref}$	40.88 mol/m ³
Reference oxygen molar concentration, $c_{O_2,ref}$	40.88 mol/m ³
Anodic and cathodic transfer coefficients for hydrogen oxidation reaction (HOR)	$\alpha_a = \alpha_c = 1$
Cathodic transfer coefficient for oxygen reduction reaction (ORR)	$\alpha_c = 1$
Dry membrane density, ρ^{mem}	2000 kg/m ³
Equivalent weight of electrolyte in membrane, EW	1.1 kg/mol
Faraday constant, F	96,487 C/mol
Universal gas constant, R_u	8.314 J/mol K
Surface tension, σ	0.0625 N/m
Contact angle of anode/cathode DM and catalyst layers, θ	110°
Liquid water density, ρ^l (80°C)	972 kg/m ³
Liquid water viscosity, μ^l	$3.5 \times 10^{-4} \text{ N} \cdot \text{s/m}^2$
Catalyst coverage coefficient, n_c	2.0
Diffusivity correction factor, n	2.3
Effective electronic conductivity in catalyst layers, σ_{CL}	1000 S/m
Effective electronic conductivity in DM, σ_{DM}	10000 S/m
Electronic conductivity in current collector, σ_{land}	20000 S/m

The DWT interfaces exhibit complex 3D topology. Figure 4 shows the 3D contours of the liquid saturation in the cathode GDL from two views. The DWT fronts are represented by the meshed iso-surfaces of $s = 1\%$. As discussed earlier, there are three different regions inside the cathode GDL: dry inlet region, wet middle region,

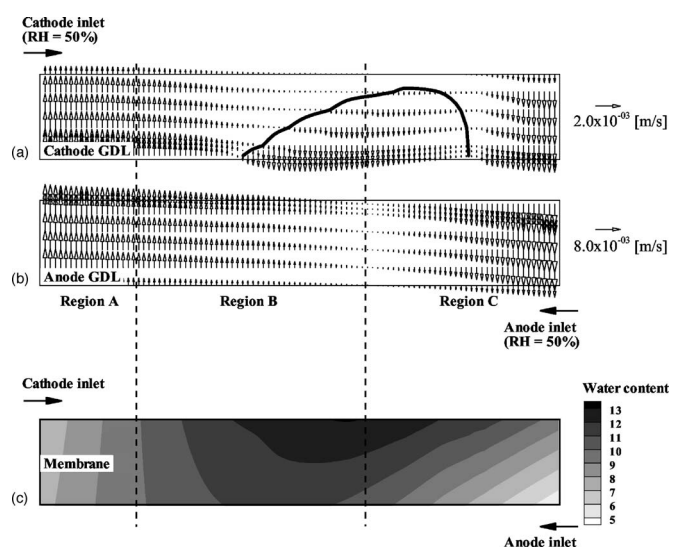


Figure 3. Gas velocity in the (a) cathode GDL, (b) anode GDL, and (c) water content distribution in the membrane along the flow direction from the center of the gas channel.

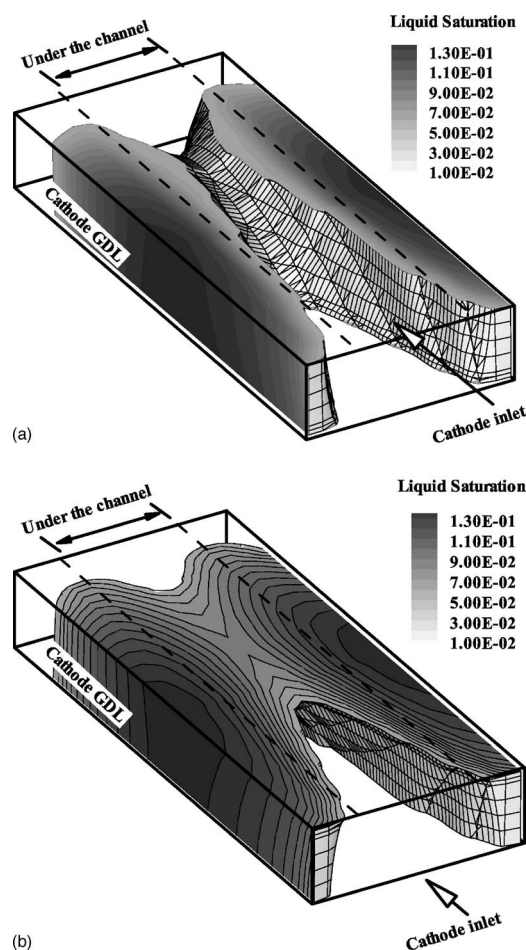


Figure 4. Liquid saturation contours in the cathode GDL. (a) The top surface is the cathode GDL/channel interface. (b) The top surface is the cathode GDL/CL interface. DWT fronts are represented by the meshed iso-surfaces of $s = 0.01$.

and dry outlet region. Figure 4 clearly shows that the two-phase zone is more extensive under the land than under the channel due to hindered water removal by the land. Liquid water appears first and disappears last in the cathode catalyst layer under the land. The maximum liquid saturation of 13% is found in the cathode catalyst layer under the land.

Figure 5 shows the 3D contours of liquid saturation in the anode GDL. The two-phase zone with the maximum liquid saturation of 4% is confined to a small area in the anode GDL under the land. There are two reasons for the formation of liquid water here. First, liquid water tends to accumulate under the land due to poor water removal. Second, the opposite side of the membrane has the highest water concentration or liquid saturation, resulting in strong back flow of water into the anode side.

The gas and liquid velocities with liquid saturation contours inside the cathode GDL are displayed in Fig. 6. In the two-phase zone, liquid water flows toward the DWT fronts, with the gas velocity in counterflow with the liquid. In the single-phase region, the direction of gas velocity is determined by the direction of net water flux across the membrane. Capable of predicting the individual velocity fields of each phase as shown in Fig. 6, the M^2 model is clearly a two-phase flow model. Compared to the traditional two-fluid model, the M^2 model is able to predict DWT accurately and efficiently, a capability yet to be demonstrated by two-fluid models.

The M^2 model is also used to explore the effect of inlet relative humidity on the location of DWT. Figure 7 shows the 3D liquid saturation contours in the cathode GDL for a case with 75% relative

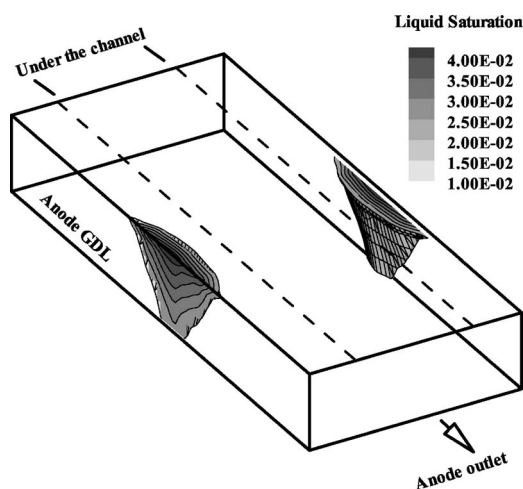


Figure 5. Liquid saturation contours in the anode GDL with the top surface being the anode GDL/CL interface and the bottom the anode GDL/channel interface. DWT fronts are represented by the meshed iso-surfaces of $s = 0.01$.

humidity at the cathode inlet. As expected, Fig. 7 shows that an increase of inlet RH results in an early appearance of liquid water in the GDLs. The DWT fronts represented by 1% saturation move outwards to the GDL/channel interface, and the maximum liquid saturation increases to 15% in the cathode. As shown in Fig. 8, the

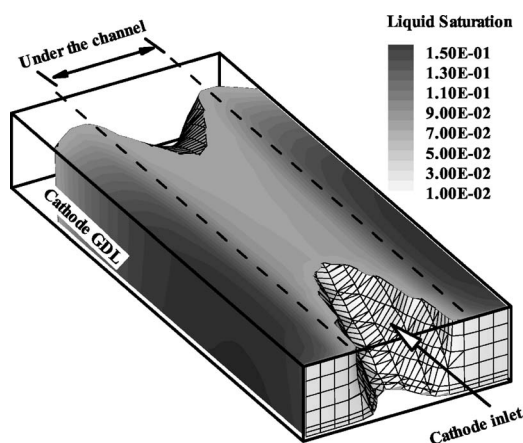


Figure 7. Liquid saturation contours in the cathode GDL with the top surface being the cathode GDL/channel interface. DWT fronts are represented by the meshed iso-surfaces of $s = 0.01$ (inlet RH: 50% anode/75% cathode).

anode two-phase zone is also extended compared to the base case. The maximum liquid saturation under the land in the anode increases to 6%, directly benefiting from higher liquid saturation on the cathode side of the membrane.

Nonisothermal two-phase calculations featuring the dry-wet-dry transition in fuel cells with more complex geometries and integrated coolant channels have been presented in Ju,¹⁵ for example.

Conclusion

Dry-wet-dry transition is an important feature of PEFCs operated under automotive conditions, and hence its accurate and efficient prediction is indispensable for any two-phase PEFC models. The present work demonstrates that the M^2 model can efficiently capture the dry-wet-dry transition in a fixed grid, making it a particularly attractive framework for computations of PEFCs. Work is ongoing to further extend the M^2 model for transient simulations of PEFCs with moving dry-to-wet fronts. We emphasize that the DWT problem is an important benchmark for PEFC code developers to test and advance future computer models.

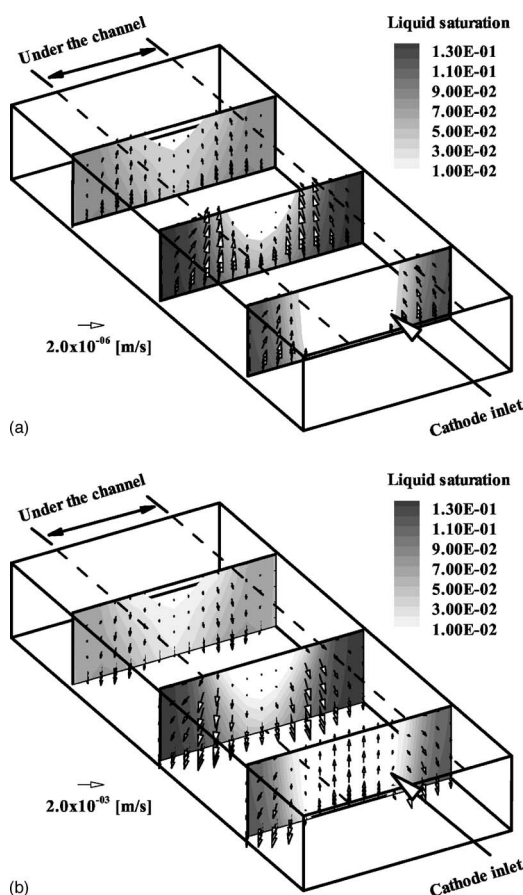


Figure 6. Liquid velocity (a) and gas velocity (b) with liquid saturation contours in the cathode GDL. The top surface is the cathode GDL/channel interface, and the bottom surface is the cathode GDL/CL interface.

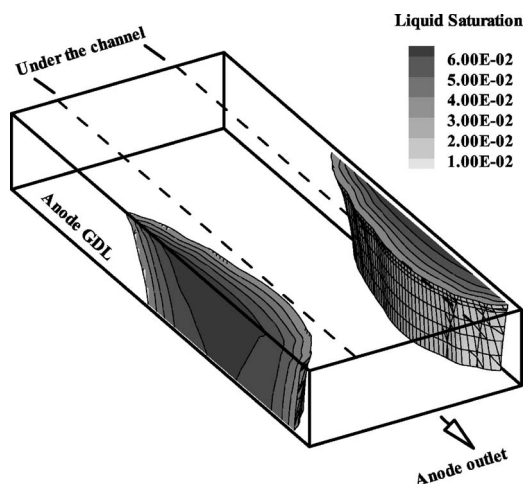


Figure 8. Liquid saturation contours in the anode GDL with the top surface being the anode GDL/CL interface and the bottom the anode GDL/channel interface. DWT fronts are represented by the meshed iso-surfaces of $s = 0.01$ (inlet RH: 50% anode/75% cathode).

Acknowledgments

Support for this work by ECEC industrial sponsors is gratefully acknowledged.

The Pennsylvania State University assisted in meeting the publication costs of this article.

References

1. J. Crank, *Free and Moving Boundary Problems*, Clarendon Press, Oxford (1984).
2. T. Berning and N. Djilali, *J. Electrochem. Soc.*, **150**, A1589 (2003).
3. S. Mazumder and J. V. Cole, *J. Electrochem. Soc.*, **150**, A1510 (2003).
4. H. Meng and C. Y. Wang, *J. Electrochem. Soc.*, **152**, A1733 (2005).
5. C. Y. Wang and P. Cheng, *Int. J. Heat Mass Transfer*, **39**, 3607 (1996).
6. Z. H. Wang, C. Y. Wang, and K. S. Chen, *J. Power Sources*, **94**, 40 (2001).
7. U. Pasaogullari and C. Y. Wang, *J. Electrochem. Soc.*, **152**, A380 (2005).
8. Y. Wang and C. Y. Wang, *J. Electrochem. Soc.*, **153**, A1193 (2006).
9. C. Y. Wang, *Chem. Rev. (Washington, D.C.)*, **104**, 4727 (2004).
10. Y. Wang and C. Y. Wang, *J. Electrochem. Soc.*, **152**, 445 (2005).
11. C. Berger, *Handbook of Fuel Cell Technology*, Prentice-Hall, Saddle River, NJ (1968).
12. T. E. Springer, T. A. Zawodinski, and S. Gottesfeld, *J. Electrochem. Soc.*, **138**, 2334 (1991).
13. STAR-CD Version 3.15, CD-Adapco Group (2001).
14. H. Meng and C. Y. Wang, *J. Electrochem. Soc.*, **151**, A358 (2004).
15. H. Ju, Ph.D. Thesis, The Pennsylvania State University (2006).